

000
001
002
003
004
005
006
007
008
009
010
011054
055
056
057
058
059
060
061
062
063
064
065
066
067
068
069
070
071
072
073
074
075
076
077
078
079
080
081
082
083
084
085
086
087
088
089
090
091
092
093
094
095
096
097
098
099
100
101
102
103
104
105
106
107

Texture Mapping 3D Models of Indoor Environments with Noisy Camera Poses

Anonymous 3DIMPVT submission

Paper ID ****

Abstract

Automated 3D modeling of building interiors is useful in applications such as virtual reality and environment mapping. Applying textures to these models is an important step in generating photorealistic visualizations of data collected by modeling systems. Camera pose recovery in such systems often suffers from inaccuracies, resulting in visible discontinuities when successive images are projected adjacently onto a plane for texturing. We propose two approaches to reduce discontinuities in texture mapping 3D models made of planar surfaces. The first one is tile based and can be used for images and planes at arbitrary angles relative to each other. The second one results in a more seamless texture, but is only applicable where camera axes for images are closely aligned with plane normals of the surfaces to be textured. The effectiveness of our approaches are demonstrated on two indoor datasets.

1. Introduction

Three-dimensional modeling of indoor environments has a variety of applications such as training and simulation for disaster management, virtual heritage conservation, and mapping of hazardous sites. Manual construction of these digital models can be time consuming, and as such, automated 3D site modeling has garnered much interest in recent years.

The first step in automated 3D modeling is the physical scanning of the environment's geometry. An indoor modeling system must be able to recover camera poses within an environment while simultaneously reconstructing the 3D structure of the environment itself [5, 13, 14, 16]. This is known as the simultaneous localization and mapping (SLAM) problem, and is generally solved by taking readings from laser range scanners, cameras, and inertial measurement units (IMUs) at multiple locations within the environment.

Mounting such devices on a platform carried by an ambulatory human provides unique advantages over vehicular-based systems on wheels in terms of agility and portability,

but can also result in larger localization error [16]. As a result, common methods for texture mapping generally produce poor results.

In this paper, we present a number of approaches to texture mapping 3D models of indoor environments made of planar surfaces in the presence of uncertainty and noise in camera poses. In particular, we consider data obtained from a human-operated backpack system with a number of laser range scanners as well as 2 cameras facing left and right, each equipped with fisheye lenses reaching an approximately 180° field of view and taking photos at a rate of 5 Hz. Applying multiple localization and loop-closure algorithms on the raw data collected by the onboard sensors [5, 14, 16], the backpack is localized¹ over its data collection period. This requires recovering the 6 degrees of freedom for the backpack as well as the cameras rigidly mounted on it. Once this is complete, the data from the laser range scanners is used to generate a 3D point cloud of the surrounding environment, from which a 3D planar model is created [20]. This model, consisting of 2D polygonal planes in 3D space, along with the set of images captured by the backpack's cameras and their noisy 3D poses, can be considered the input to our texture mapping problem.

This problem straddles the fields of image-based localization refinement as well as image alignment and mosaicing, and thus our proposed solution shares many similarities with past research in those areas, which will be examined in Section 3. However, we can exploit known approximate camera poses as well as the 3D geometry of the environment to more accurately and efficiently texture the planes.

The remainder of the paper is organized as follows. Section 2 describes two variants of a tile-based mapping approach and their shortcomings. Section 3 discusses past research in related fields, demonstrates two previous attempts at improving texture alignment, and exhibits their inadequacies for our datasets. Section 4 presents our proposed seam minimization approach to texture mapping. Section 5 contains results and conclusions.

In all subsequent sections, we discuss the process of tex-

¹In this paper, we use the terms localization and pose recovery interchangeably, in that they both refer to recovering position and orientation.

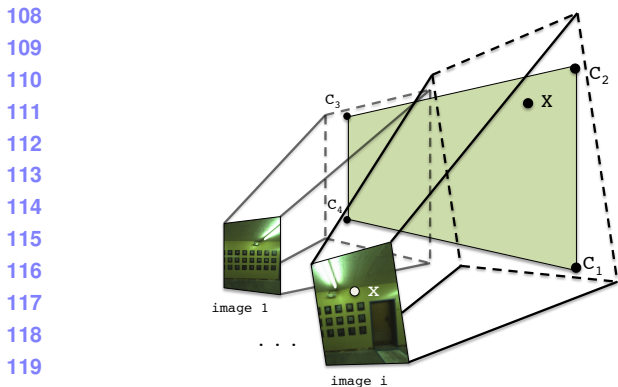


Figure 1: Planes are specified in 3D space by four corners C_1 to C_4 . Images are related to each plane through the camera matrices $P_{1..M}$.

ture mapping a single plane, as the texturing of each plane is independent and can be completed in parallel.

2. Tile-Based Texture Mapping

The geometry of the texture mapping process for a plane is shown in Figure 1. As described earlier, we are provided with a set of M images to texture the target plane. Each image has a camera matrix P_i for $i = 1..M$, which translates a 3D point in the world coordinate system to a 2D point or pixel in image i 's coordinates. A camera matrix P_i is composed of the camera's intrinsic parameters, such as focal length and image center, as well as extrinsic parameters which specify the rotation and translation of the camera's position in 3D world coordinates at the time that image i is taken. These extrinsic parameters are determined by the backpack hardware and localization algorithms [5, 16, 14] and are quite noisy.

Because the backpack system takes photos at a rate of 5 Hz, thousands of images are available for texturing each plane. Our goal in creating a texture mapping process is to decide which of these images should be used, and where their contents should map onto the texture, in order to eliminate any visual discontinuities or seams that would suggest that the plane's final texture is not composed of a single continuous image.

2.1. Direct Mapping

Ignoring the fact that the camera matrices $P_{1..M}$ are inaccurate, we can texture the plane by discretizing it into small square tiles, generally about 5 pixels across, and choosing an image to texture each tile.

We choose to work with rectangular units to ensure that borders between any two distinct images in the final texture are either horizontal or vertical. Since most environmental features inside buildings are horizontal or vertical, any

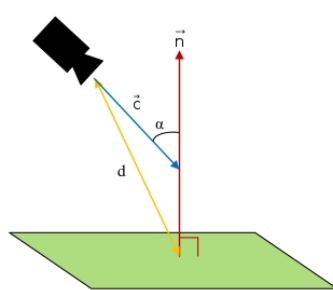


Figure 2: We minimize camera angle α and distance d by maximizing the scoring function $\frac{1}{d}(-1 \cdot \vec{c}) \cdot \vec{n}$

seams in our texture intersect them minimally and are likely to be less noticeable.

In order to select an image for texturing a tile t , we must first gather a list of candidate images that contain all four of its corners, which we can quickly check by projecting t into each image using the P_i camera matrices. Furthermore, each candidate image must have been taken at a time when its camera had a clear line-of-sight to t , which can be calculated using standard ray-polygon intersection tests between the camera location, the center of t , and every other plane [11].

Once we have a list of candidate images for t , we define a scoring function in order to objectively select the best image. Since camera pose errors compound over distance, we wish to minimize the distance between cameras and the plane they texture. Additionally, we desire images that are projected perpendicularly onto the plane, maximizing the resolution and amount of useful texture available in their projections, as well as minimizing any parallax effects. In other words, we wish to minimize the angle between the plane normal and the camera axis for images selected for texture mapping. These two criteria can be met by maximizing the function $\frac{1}{d}(-1 \cdot \vec{c}) \cdot \vec{n}$ as shown in Figure 2. Specifically, d is the distance between the centers of a camera and a tile, and \vec{n} and \vec{c} are the directions of the plane's normal and the camera axis respectively.

As Figure 3(a) demonstrates, this approach leads to the best texture for each tile independently, but overall results in many image boundaries with abrupt discontinuities, due to significant misalignment between images, as a result of camera pose inaccuracies.

2.2. Mapping with Caching

Since discontinuities occur where adjacent tiles select non-aligned images, it makes sense to take into account image selections made by neighboring tiles while texture mapping a given tile. By using the same image across tile boundaries, we can eliminate a discontinuity altogether. If this is not possible because a tile is not visible in images chosen by its neighbors, using similar images across tile

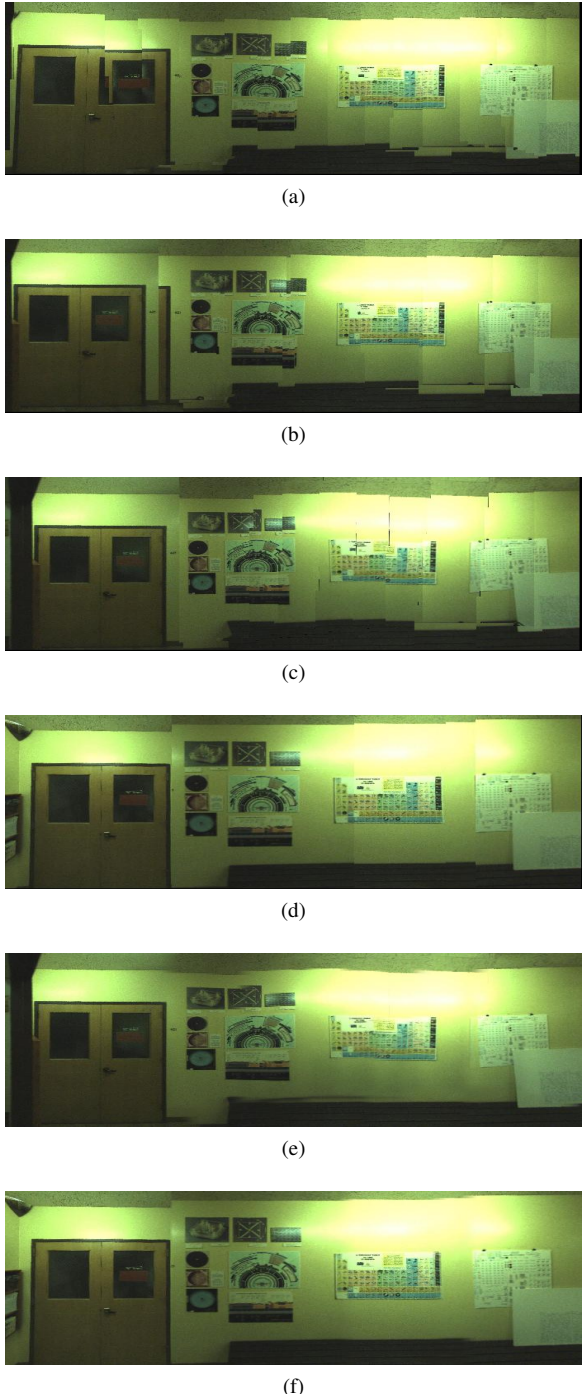


Figure 3: (a) Direct mapping. (b) Mapping with caching. (c) Mapping with caching after image alignment. (d) Seam minimization after image alignment. (e) same as (c) with blending. (f) same as (d) with blending.

boundaries also leads to less noticeable discontinuities.

Similar to a caching mechanism, we select the best image for a tile t by searching through two subsets of images

for a viable candidate, before searching through the entire set. The first subset of images is those selected by adjacent tiles that have already been textured. We must first check which of these images can map to t , and then of those, we make a choice according to the scoring function in Figure 2. Before reusing this image, we ensure it meets the criteria $\alpha < 45^\circ$, in order to be considered a viable image, with α as the camera angle as shown in Figure 2.

If no satisfactory image is found in the first subset, we check the second subset of images, consisting of those taken near the ones in the first subset, both spatially and temporally. These images are not the same as the ones used for neighboring tiles, but are taken at a similar location and time, suggesting that their localization and projection are quite similar. Again, if no viable image is found according to the same criteria, we search the entire set of candidate images, selecting based on the same scoring function from Figure 2.

The result of this caching approach is shown in Figure 3(b). As compared to Figure 3(a), discontinuities are reduced overall, but the amount of remaining seams suggests that image selection alone cannot produce seamless textures. Camera matrices, or the image projections themselves have to be adjusted in order to reliably generate clean textures.

3. Existing Approaches to Image Alignment

In order to produce seamless texture mapping, either camera matrices need to be refined such that their localization is pixel accurate, or image stitching techniques need to be applied to provide this illusion.

Image projections can be aligned by refining their noisy camera poses, using image correspondences to adjust each image's camera matrix over 6 degrees of freedom (DOF) [7, 16, 21, 24]. Applying such approaches to our datasets however results in error accumulation and drift as shown in Figure 4(a), as well as high complexity and runtime [16].

Another common approach to image alignment is to iteratively match images on intensity differences in selected patches, often in a spatial hierarchy [12, 18, 21, 23]. Another widely-used approach is to perform feature matching, which requires the detection of visual features and their existence in multiple images [4, 6, 19, 23, 26]. Notably, both approaches rely on the presence of multiple visual references, as when texturing detailed objects at high resolutions [2, 25], or when creating large scene panoramas [1, 2, 8, 22]. In contrast, our indoor datasets have a high prevalence of bare walls and ceilings, resulting in few reference points that can be used to judge alignment.

Additionally, our datasets often contain long chains of images, which leads to error accumulation when image correspondences are not accurate. For example, when matching a long chain of images through homography, a pixel in

270
271
272
273
274
275
276
277
278
279
280
281
282
283
284
285
286
287
288
289
290
291
292
293
294
295
296
297
298
299
300
301
302
303
304
305
306
307
308
309
310
311
312
313
314
315
316
317
318
319
320
321
322
323



(a)



(b)

Figure 4: Texture alignment via (a) the graph-based localization refinement algorithm from [5] and (b) image mosaicing

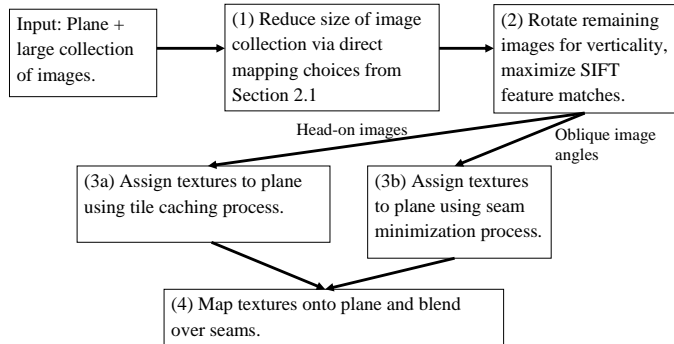


Figure 5: Our proposed method for seamless texture mapping.

the n th image must be translated into the first image's coordinates by multiplying by the 3×3 matrix $H_1H_2H_3\dots H_n$. Any error in one of these homography matrices is propagated to all further images, resulting in drift. Figure 4(b) shows the output of the AutoStitch software package, which performs homography-based image mosaicing [3]. Even with many features spread across this plane, the mosaicing produces errors that causes straight lines to appear as waves on the plane, despite the fact that it is generated after careful hand tuning. Many planes with fewer features simply failed outright using this approach.

4. Seamless Texture Mapping

In this section, we describe our proposed method for seamless texture mapping. Our approach consists of 4 steps, as seen in Figure 5. First, we choose a subset of M images to work with via the direct mapping approach of Section 2.1. Next, we project these images onto the plane and perform rotation and shifting in order to maximize SIFT feature

matches in overlapping areas between these projections. We then select which textures to be used either with the tile caching method from Section 2.2, or with the more specialized method to be described in Section 4.3. This choice depends on the availability of head-on images for a given plane. We then finish by applying linear alpha blending to smooth out any remaining seams.

4.1. Image Rotation

We begin with the projection of all images onto the plane. This is done in the same way as in Section 2. Rather than work with all 6 DOF, which is computationally intensive, we choose to work only in two dimensions, performing 2D rotations and translations on the image projections, as errors in either lead to the greatest discontinuities.

We perform rotations using Hough transforms, which detect the presence and orientation of linear features in our images. Rather than match the orientation of such features in each image, we simply apply rotations such that the strongest near-vertical features are made completely vertical. This is effective for vertical planes in indoor models, since they usually consist of parallel vertical lines corresponding to doors, wall panels, rectangular frames, etc. If features in the area are not vertical, e.g. for floors and ceilings, this step is skipped.

4.2. Image Shifting

Our next step is to align overlapping images by searching for corresponding points between all pairs of overlapping images. We use SIFT features for their high detection rate, and choose to use feature alignment rather than intensity-based alignment due to the differences in lighting as well as possible occlusion among our images, both of which feature alignment is less sensitive to [15, 17, 19, 23].

SIFT matches determine d^x and d^y distances between each pair of features for two images on the plane, though these distances may not always be the same for different features. Since indoor environments often contain repetitive features such as floor tiles or doors, we need to ensure that SIFT-based distances are reliable. In order to mitigate the effect of incorrect matches and outliers, the RANSAC framework [10] is used for a robust estimate of the optimal $d_{i,j}^x$ and $d_{i,j}^y$ distances between two images i and j . The RANSAC framework handles the consensus-building machinery, and requires a fitting function and a distance function. For this application, the fitting function simply finds the average distance between matches in a pair of images. The distance function for a pair of points is chosen to be the difference between those points' SIFT match distance and the average distance computed by the fitting function. We use a 10 pixel outlier threshold, so that SIFT matches are labeled as outliers if their horizontal or vertical distances are not within 10 pixels of the average distance computed by

378

379

380

381

382

383

384

385

386

387

388

389

390

391

392

393

394

395

396

397

398

399

400

401

402

403

404

405

406

407

408

409

410

411

412

413

414

415

416

417

418

419

420

421

422

423

424

425

426

427

428

429

430

431

432

the fitting function.

433

We now use the $d_{i,j}^x$ and $d_{i,j}^y$ distances between each pair of images to refine their positions using least squares. Recall that there are a total of M^2 possible pairs of images, though we only generate distances between images that overlap at SIFT feature points. Given these distances and the original image location estimates, we can solve a least squares problem ($\min_{\vec{\beta}} \|A\vec{\beta} - \vec{\gamma}\|_2^2$) to estimate the location of the images on the plane. The M -dimensional vector $\vec{\beta}$ represents the unknown x location of each image on the plane for $1 \dots M$. The optimal x and y locations are obtained in the same way, so we only consider the x locations here:

445

$$\vec{\beta} = (x_1, x_2, x_3, \dots, x_{M-1}, x_M)$$

446

The $N \times (M + 1)$ dimensional matrix A is constructed with one row for each pair of images with measured distances produced by the SIFT matching stage. A row in the matrix has a -1 and 1 in the columns corresponding to the two images in the pair. For example, the matrix below indicates a SIFT-based distance between images 1 and 2, images 1 and 3, images 2 and 3, etc.

456

$$A = \begin{pmatrix} -1 & 1 & 0 & \dots & 0 & 0 \\ -1 & 0 & 1 & \dots & 0 & 0 \\ 0 & -1 & 1 & \dots & 0 & 0 \\ \vdots & \vdots & \vdots & \ddots & \vdots & \vdots \\ 0 & 0 & 0 & \dots & 1 & 0 \\ 0 & 0 & 0 & \dots & -1 & 1 \\ 1 & 0 & 0 & \dots & 0 & 0 \end{pmatrix}$$

465

If only relative distances between images are included then there is no way to determine the absolute location of any of the images and the matrix becomes rank deficient. To fix this we choose the first image to serve as the anchor for the rest, meaning all the absolute distances are based on its original location. This is done by adding a row with a 1 in the first column and the rest zeros.

472

Finally, the N -dimensional observation vector $\vec{\gamma}$ is constructed using the SIFT-based distances generated earlier in the RANSAC matching stage. The last element in the observation vector is the location of the first image determined by its original noisy localization, from [5, 16]. Thus $\vec{\gamma}$ can be written as:

478

$$\vec{\gamma}^T = (d_{1,2}, d_{1,3}, d_{2,3}, \dots, d_{N-2,N-1}, d_{N-1,N}, x_1)$$

481

The $\vec{\beta}$ that minimizes $\|A\vec{\beta} - \vec{\gamma}\|_2^2$ results in a set of image locations on the plane that best honors all the SIFT-based distance measurements between images. In practice there is often a break in the chain of images, meaning that no

486

487

488

489

490

491

492

493

494

495

496

497

498

499

500

501

502

503

504

505

506

507

508

509

510

511

512

513

514

515

516

517

518

519

520

521

522

523

524

525

526

527

528

529

530

531

532

533

534

535

536

537

538

539

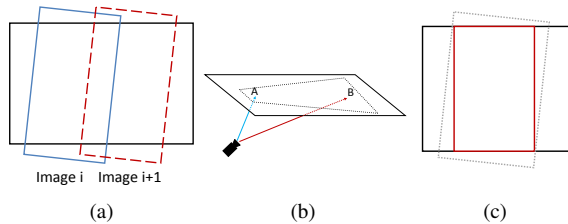


Figure 6: (a) Undistorted fisheye images for vertical planes are tilted, but their effective camera axis is more or less normal to the plane. (b) The effective camera axis for ceilings is at an angle with respect to the plane normal. (c) Wall images are cropped to be rectangular.

SIFT matches are found between one segment of the plane and another. In this case we add rows to the A matrix and observations to the $\vec{\gamma}$ vector that contain the original noisy x and y distance estimates from the original camera poses. Another way to do this is to add rows for all neighboring pairs of images and solve a weighted least squares problem where the SIFT distances are given a higher weight i.e. 1, and the noisy distances generated by the original camera poses [5, 16] are given a smaller weight e.g. 0.01.

After completing this same process for the y dimension as well, and making the resultant shifts, our images overlap and match each other with far greater accuracy. Applying the tile caching method from Section 2.2 on these rotated and shifted images results in the significant improvements shown in Figure 3(c), as compared to Figure 3(b).

4.3. Seam Minimization

As mentioned earlier, the mobile backpack system used to capture data in this paper contains 2 cameras with 180° fisheye lenses facing to the right and left. Since most human operators do not carry the backpack in a perfectly upright position and are bent forwards at 15 to 20 degrees with respect to the vertical direction, the undistorted fisheye images are head on with respect to vertical walls, but at an angle with respect to horizontal floors and ceilings. This is depicted for wall and ceiling planes in Figures 6(a) and 6(b) respectively. These oblique camera angles for ceilings translate into textures that span extremely large areas once projected, as shown in Figure 6(b). Using the tile-based texture mapping criteria from Figure 2, such projections have highly varying scores depending on the location on the plane, as shown in Figure 6(b). Thus, the tiling approach in Section 2 is a reasonable choice for texturing floors and ceilings, as it uses the parts of image projections that are viable choices for their respective plane locations, e.g. areas near point A in Figure 6(b), but not near point B.

For wall planes however, most images are taken from close distances and more or less head-on angles, resulting

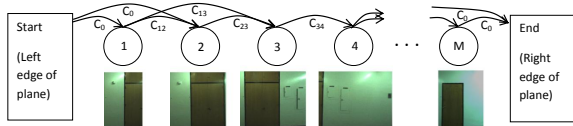


Figure 7: DAG construction for the image selection process.

in higher resolution fronto-parallel projections. As a result, for each tile on a wall plane, the scoring function of Figure 2 is relatively flat with respect to a large number of captured images, as they are all more or less head on. Thus, the scoring function is less significant for walls, and it is conceivable to use a different texturing strategy for them so as to minimize visible seams in texture mapped planes. This can be done by choosing the smallest possible set of images that (a) covers the entire plane and (b) minimizes the amount of visible seams between them. A straightforward cost function that accomplishes the latter is the Sum of Squared Differences (SSD) of pixels in overlapping regions between all pairs of images, after they have been rotated as described in Section 4.1. Minimizing this cost function encourages image boundaries to occur either in featureless areas, such as bare walls, or in areas where images match extremely well.

To cover the entirety of a plane, our problem can be defined as minimally covering a polygon i.e. the plane, using other polygons of arbitrary geometry i.e. image projections, with the added constraint of minimizing the cost function between chosen images. This is a complex problem, though we can take a number of steps to simplify it. Given that wall-texture candidate images are taken from more or less head-on angles, and assuming only minor rotations are made in Section 4.1, we can reason that their projections onto the plane are approximately rectangular. By cropping them all to be rectangular, as shown in Figure 6(c), our problem becomes the conceptually simpler one of filling a polygon with rectangles, such that the sum of all costs between each pair of rectangles is minimal. We thus also retain the advantages of working with rectangular units, as explained in Section 2.

The location and orientation of the cameras and the fish-eye lenses on the acquisition backpack is such that images nearly always contain the entirety of the floor to ceiling range of wall planes. Images are therefore rarely projected with one above another when texturing wall planes. In essence, we need only to ensure lateral coverage of wall planes, e.g. from left to right, as our images provide full vertical coverage themselves. We can thus construct a Directed Acyclic Graph (DAG) from the images, with edge costs defined by the SSD cost function, and solve a simple shortest path problem to find an optimal subset of images with regard to the cost function [9].

Figure 7 demonstrates the construction of a DAG from

overlapping images of a long hallway. Images are sorted by horizontal location left to right, and become nodes in a graph. Directed edges are placed in the graph from left to right between overlapping images. The weights of these edges are determined by the SSD cost function. Next, we add two artificial nodes, one start node representing the left border of the plane, and one end node representing the right border of the plane. The left(right) artificial node has directed edges with equal cost C_0 to(from) all images that meet the left(right) border of the plane.

We now solve the shortest path problem from the start node to the end node. This results in a set of images completely covering the plane horizontally, while minimizing the cost of seams between images.

In rare cases where the vertical dimension of the plane is not entirely covered by one or more chosen images, we are left with holes where no images are selected to texture. To address this, we solve for a new shortest path after modifying the edges chosen by the original shortest path solution such that they have higher cost than all other edges in the DAG, and solve for a new shortest path. This ensures that these edges are not chosen again unless they are the only available option. Our second shortest path solution results in a new set of chosen images, of which we only retain those that cover areas not covered by the first set. This process can be repeated as many times as needed, until holes are no longer present. This method is not as optimal as a 2D-coverage solution would be, but it is a fast approximation, and adequately handles the few holes we encounter.

With this completed, we have now mapped every location on the plane to at least one image, and have minimized the number of images, as well as the discontinuities between their borders. As seen in Figure 3(d), this seam minimization method has fewer visible discontinuities than Figure 3(c) corresponding to the tile caching approach². This is especially evident when comparing the posters in the images, which have clear misalignment over seams in Figure 3(c), but are much more aligned in Figure 3(d). This is because the seam minimization approach directly reduces the cost of each image boundary, while the tile caching method uses a scoring function that only approximates this effect. Furthermore, seam minimization guarantees the best selection of images, while the sequential tile caching method may select images early on that turn out to be poor choices once subsequent tiles have been processed. The seam minimization approach is also far less intensive in terms of memory usage and runtime, both during texture generation and rendering, as it does not require discretizing planes or images³.

²In Figure 3(d), we arbitrarily chose one image for texturing where images overlap, as blending will be discussed in the next section.

³For the seam minimization process, it is important that images only contain content that should be mapped onto the target plane in question. The tiling approach checks occlusion for each tile as it is being textured, whereas the seam minimization approach uses entire images. Occlusion

648 In the context of texturing an entire 3D planar model, we
 649 choose to apply the seam minimization approach on walls,
 650 due to its superior output when provided with head-on im-
 651 ages. Floors and ceilings however, given their many images
 652 taken at oblique angles, are textured using the tile caching
 653 method.
 654

655 4.4. Blending

656 We now apply the same blending process to the two tex-
 657 turing methods: image alignment followed by either tile
 658 caching or seam minimization.
 659

660 Although the preprocessing steps and image selection in
 661 both methods attempt to minimize all mismatches between
 662 images, there are occasional unavoidable discontinuities in
 663 the final texture due to different lighting conditions or inac-
 664 curacies in planar geometry or projection. These can how-
 665 ever be treated and smoothed over by applying alpha blend-
 666 ing over image seams. Whether the units we are blending
 667 are rectangularly-cropped images or rectangular tiles, we
 668 can apply the same blending procedure, as long as we have
 669 a guaranteed overlap between units to blend over.
 670

671 For the tile caching method, we can ensure overlap by
 672 texturing a larger tile than needed for display. For exam-
 673 ple, for a rendered tile $l_1 \times l_1$, we can associate it with a
 674 texture $(l_1 + l_2) \times (l_1 + l_2)$ in size. For the seam mini-
 675 mization method, we have already ensured overlap between
 676 images. To enforce consistent blending however, we add a
 677 minimum required overlap distance while solving the
 678 shortest path problem in Section 4.3. Additionally, if im-
 679 ages overlap in a region greater than the overlap distance,
 680 we only apply blending over an area equal to the overlap
 681 distance.
 682

683 After blending pixels linearly across overlapping regions
 684 using alpha blending, texture mapping is complete. Figures
 685 3(e) and 3(f) show the blended versions of Figures 3(c) and
 686 3(d) respectively. It is clear that the seam minimization
 687 approach still exhibits better alignment and fewer seams than
 688 the tile-caching method, as Figure 3(f) has the best visual
 689 quality among the textures in Figure 3.
 690

691 5. Results and Conclusions

692 Examples of ceilings and floors textured with the tile
 693 caching approach, and walls textured with the seam mini-
 694 mization approach, are displayed in Figure 8. High reso-
 695 lution texture comparisons, as well as a walkthrough of a
 696 fully textured 3D model are available in the accompanying
 697 video to this paper.
 698

699 In this paper, we have developed an approach to texture
 700 map models with noisy camera localization data. We are
 701 able to refine image locations based on feature matching,

checks thus need to be performed over the entirety of each image to determine available areas for texture mapping a given plane.

702 and robustly handle outliers. The tile-based mapping ap-
 703 proach can be used to texture both simple rectangular walls
 704 as well as complex floor and ceiling geometry. We also pre-
 705 sented a seam minimization texturing method that produces
 706 seamless textures on planes where multiple head-on images
 707 are available. Each of these approaches is highly modular,
 708 and easily tunable for different environments and acquisi-
 709 tion hardware.
 710

711 References

- [1] A. Agarwala, M. Agrawala, M. Cohen, D. Salesin, and R. Szeliski. Photographing long scenes with multi-viewpoint panoramas. In *ACM Transactions on Graphics (TOG)*, volume 25, pages 853–861. ACM, 2006. [3](#)
- [2] F. Bernardini, I. Martin, and H. Rushmeier. High-quality texture reconstruction from multiple scans. *Visualization and Computer Graphics, IEEE Transactions on*, 7(4):318–332, 2001. [3](#)
- [3] M. Brown and D. Lowe. Autostitch. <http://www.cs.bath.ac.uk/brown/autostitch/autostitch.html>. [4](#)
- [4] M. Brown and D. Lowe. Automatic panoramic image stitching using invariant features. *International Journal of Computer Vision*, 74(1):59–73, 2007. [3](#)
- [5] G. Chen, J. Kua, S. Shum, N. Naikal, M. Carlberg, and A. Zakhor. Indoor localization algorithms for a human-operated backpack system. In *Int. Symp. on 3D Data, Processing, Visualization and Transmission (3DPVT)*. Citeseer, 2010. [1, 2, 4, 5](#)
- [6] S. Cho, Y. Chung, and J. Lee. Automatic image mosaic system using image feature detection and taylor series. In *Proceedings of the 7th International Conference on Digital Image Computing: Techniques and Applications*, pages 549–556, 2003. [3](#)
- [7] S. Coorg and S. Teller. Matching and pose refinement with camera pose estimates. In *Proceedings of the 1997 Image Understanding Workshop*, 1997. [3](#)
- [8] P. Debevec, Y. Yu, and G. Borshukov. Efficient view-dependent image-based rendering with projective texture-mapping. In *Eurographics Rendering Workshop*, volume 98, pages 105–116, 1998. [3](#)
- [9] E. Dijkstra. A note on two problems in connexion graphs. *Numerische Mathematik*, 1:269–271, 1959. [6](#)
- [10] M. Fischler and R. Bolles. Random sample consensus: a paradigm for model fitting with applications to image analysis and automated cartography. *Communications of the ACM*, 24(6):381–395, 1981. [4](#)
- [11] A. Glassner et al. *An introduction to ray tracing*. Academic Press, 1989. [2](#)
- [12] G. Hager and P. Belhumeur. Efficient region tracking with parametric models of geometry and illumination. *Pattern Analysis and Machine Intelligence, IEEE Transactions on*, 20:1025–1039, 1998. [3](#)
- [13] R. Hartley and A. Zisserman. *Multiple view geometry in computer vision*, volume 2. Cambridge Univ Press, 2000. [1](#)

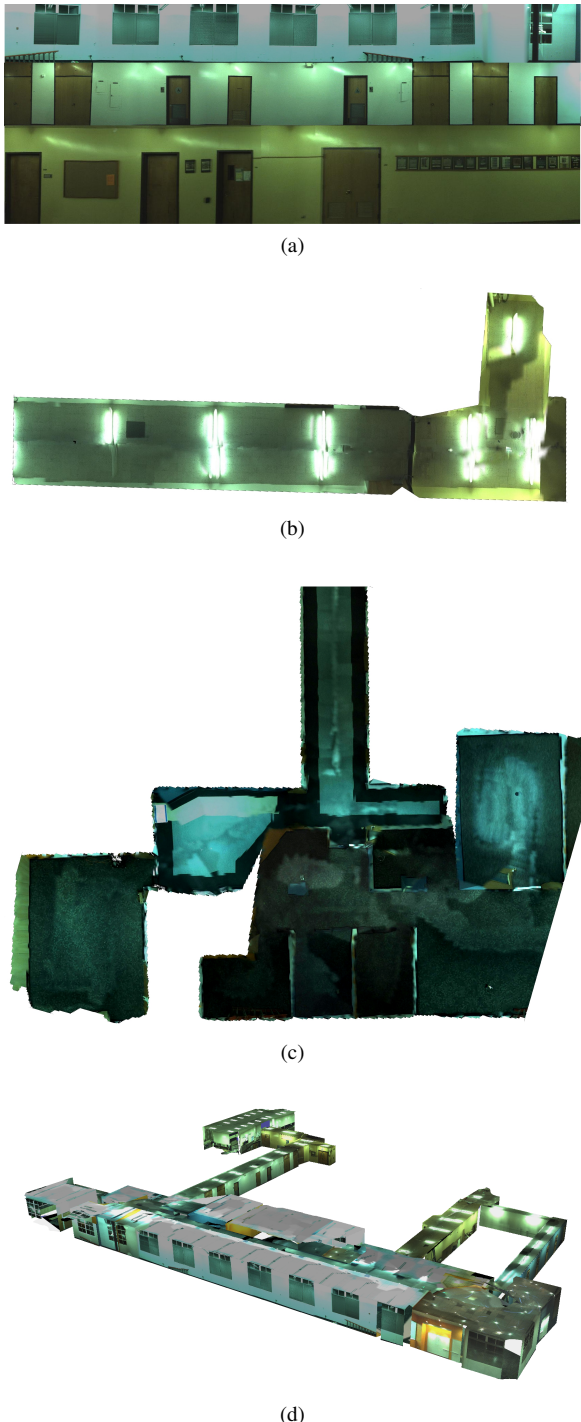


Figure 8: Examples of our final texture mapping output for (a) walls, (b) a ceiling, (c) an entire floor, (d) a full model.

- [14] J. Kua, N. Corso, and A. Zakhor. Automatic loop closure detection using multiple cameras for 3d indoor localization. In *IS&T/SPIE Electronic Imaging*, 2012. 1, 2
- [15] S. Lai and M. Fang. Robust and efficient image alignment

- with spatially varying illumination models. In *Computer Vision and Pattern Recognition, 1999. IEEE Computer Society Conference on*, volume 2. IEEE, 1999. 4
- [16] T. Liu, M. Carlberg, G. Chen, J. Chen, J. Kua, and A. Zakhor. Indoor localization and visualization using a human-operated backpack system. In *Indoor Positioning and Indoor Navigation (IPIN), 2010 International Conference on*, pages 1–10. IEEE, 2010. 1, 2, 3, 5
 - [17] D. Lowe. Object recognition from local scale-invariant features. In *Computer Vision, 1999. The Proceedings of the Seventh IEEE International Conference on*, volume 2, pages 1150–1157. Ieee, 1999. 4
 - [18] B. Lucas and T. Kanade. An iterative image registration technique with an application to stereo vision. In *Proceedings of the 7th international joint conference on Artificial intelligence*, 1981. 3
 - [19] K. Mikolajczyk and C. Schmid. A performance evaluation of local descriptors. *Pattern Analysis and Machine Intelligence, IEEE Transactions on*, 27(10):1615–1630, 2005. 3, 4
 - [20] V. Sanchez and A. Zakhor. Planar 3d modeling of building interiors from point cloud data. In *International Conference on Image Processing*, 2012. 1
 - [21] H. Shum and R. Szeliski. Systems and experiment paper: Construction of panoramic image mosaics with global and local alignment. *International Journal of Computer Vision*, 36:101–130, 2000. 3
 - [22] N. Snavely, S. Seitz, and R. Szeliski. Photo tourism: exploring photo collections in 3d. In *ACM Transactions on Graphics (TOG)*, volume 25, pages 835–846. ACM, 2006. 3
 - [23] R. Szeliski. Image alignment and stitching: A tutorial. *Foundations and Trends® in Computer Graphics and Vision*, 2(1):1–104, 2006. 3, 4
 - [24] R. Szeliski and H. Shum. Creating full view panoramic image mosaics and texture-mapped models. In *SIGGRAPH 95*, pages 251–258. ACM SIGGRAPH, 1997. 3
 - [25] L. Wang, S. Kang, R. Szeliski, and H. Shum. Optimal texture map reconstruction from multiple views. In *Computer Vision and Pattern Recognition, 2001. CVPR 2001. Proceedings of the 2001 IEEE Computer Society Conference on*, volume 1, pages I–347. IEEE, 2001. 3
 - [26] G. Yun Tian, D. Gledhill, and D. Taylor. Comprehensive interest points based imaging mosaic. *Pattern recognition letters*, 24:1171–1179, 2003. 3